Earth Planet. Sci. Lett. 641 (2024) 118802

Contents lists available at ScienceDirect

Earth and Planetary Science Letters

journal homepage: www.elsevier.com/locate/epsl

Coupled atmosphere-ocean response of the southwest Pacific to deglacial changes in Atlantic meridional overturning circulation

Shaun R. Eaves [a,b,*], Andrew N. Mackintosh [c], Joel B. Pedro [d,e], Helen C. Bostock [f], Matthew T. Ryan [a,b], Kevin P. Norton [b], Bruce W. Hayward [g], Brian M. Anderson [a], Feng He [h], Richard S. Jones [c], Andrew M. Lorrey [i], Rewi M. Newnham [b], Stephen G. Tims [j], Marcus J. Vandergoes [k]

[a] Antarctic Research Centre, PO Box 600, Victoria University of Wellington, Wellington 6140, New Zealand
[b] School of Geography, Environment, and Earth Science, Victoria University of Wellington, Wellington, New Zealand
[c] Securing Antarctica's Environmental Future, School of Earth, Atmosphere and Environment, Monash University, Australia
[d] Australian Antarctic Division, Channel Highway, Kingston, Tasmania 7050, Australia
[e] Australian Antarctic Program Partnership, Institute for Marine and Antarctic Studies, University of Tasmania, Hobart, Tasmania, Australia
[f] School of the Environment, The University of Queensland, St Lucia 4072, Queensland, Australia
[g] Geomarine Research, 19 Debron Ave, Remuera, Auckland, New Zealand
[h] Center for Climatic Research, Nelson Institute for Environmental Studies, University of Wisconsin–Madison, Madison, WI 53706, USA
[i] National Institute of Water and Atmospheric Research, Auckland, New Zealand
[j] Department of Nuclear Physics and Accelerator Applications, Research School of Physics, The Australian National University, Canberra, ACT 0200, Australia
[k] GNS Science, P.O. Box 30368, Lower Hutt 5040, New Zealand

ARTICLE INFO

Editor: Dr Y Asmerom

Keywords:
Mountain glacier
Last glacial termination
Southern hemisphere
Sea surface temperature
Bipolar seesaw
Southern westerly winds

ABSTRACT

The last glacial termination was characterised by millennial-scale episodes of warming and cooling that appear offset between the hemispheres. It has been proposed that this bi-polar seesaw is the result of climate system feedbacks. A key debate, which remains unresolved, concerns the relative roles of the atmosphere and oceans in transmitting these climate responses between the hemispheres. In this study we present quantitative climate proxy data to show that air temperatures in New Zealand, as recorded by mountain glaciers, tracked millennial-scale warming and cooling of local surface temperatures of the adjacent Tasman Sea throughout the last glacial termination. Both realms were dominated by warming between 18 ka and 12 ka, interrupted by a multi-centennial to millennial-scale cooling event centred on 14 ka, coincident with the Antarctic Cold Reversal. Reconciling our climate proxy evidence with a transient climate model simulation of the glacial termination, we find that the timing and amplitude of temperature changes are consistent with changing Atlantic meridional overturning circulation (AMOC). The southwest Pacific region displays a particularly sensitive response to AMOC intensity changes, despite its far-field situation from the North Atlantic. This sensitivity represents the combined impact of fast-acting oceanic teleconnections and regional atmosphere-ocean response associated with changes to the southern westerly winds. Our findings highlight that recent hypotheses promoting the role of southern westerlies as a critical component of deglaciation may be complementary to, rather than competitive with, the bipolar seesaw paradigm.

1. Introduction

The last glacial termination (19–11 ka; Denton et al., 2010) affords a useful natural experiment to examine the integrated climate system response to sustained global warming. Synchronised high-resolution ice core records suggest that millennial-scale climate changes during this interval were offset between the poles (WAIS Divide Project Members, 2015). Redistribution of oceanic heat between the hemispheres via changes in the intensity of the Atlantic meridional overturning circulation (AMOC; Stocker and Johnsen, 2003; McManus et al., 2004; Pedro et al., 2016), commonly referred to as the oceanic bipolar seesaw, is the leading hypothesis to explain this large-scale hemispheric variability.

* Corresponding author.
E-mail address: shaun.eaves@vuw.ac.nz (S.R. Eaves).

https://doi.org/10.1016/j.epsl.2024.118802
Received 4 December 2023; Received in revised form 20 May 2024; Accepted 22 May 2024
Available online 8 June 2024

However, more recent work has promoted the influence of shifts in atmospheric circulation, either working in tandem with AMOC-induced oceanic changes (Pedro et al., 2018; Buizert et al., 2018) or independently (Denton et al., 2021). The latter hypothesis, known as the Zealandia Switch and rooted in southern hemisphere climate proxy observations and supported by climate model experiments, suggests a negligible role for AMOC as a global climate driver during deglaciation (Denton et al., 2022). Instead, this theory suggests that sustained shifts in the southern westerly winds and the associated impact on tropical export are the primary influence on Earth's thermal balance during this interval, while any AMOC-related climate impacts were restricted to the winter season in the North Atlantic (Denton et al., 2022; Putnam et al., 2023). Understanding the role of AMOC as the driver of global-scale climate variability is of high importance given recent observed and predicted future changes in this key component of global oceanic circulation (Caesar et al., 2021; Ditlevsen and Ditlevsen, 2023).

In this study, we test the competing hypotheses concerning AMOC's relative role in driving the glacial termination and global climate variability using an integrated marine- and terrestrial-climate proxy approach in the New Zealand region. Situated far from the high latitudes of the North Atlantic where AMOC effects dominate, we reason that our southwest Pacific study region is well placed to test the potential global reach of AMOC teleconnections. Furthermore, climate variability in the southwest Pacific is sensitive to changes in oceanic and atmospheric circulation due to its mid-latitude, maritime setting, which is principally controlled by the relative influence of subpolar and subtropical air and water masses (Fig. 1). The position and intensity of the southern hemisphere westerly winds fundamentally controls regional oceanographic conditions including the position of the fronts and ocean circulation and thus regional heat distribution around the southern continents (Hall and Visbeck, 2002; Gupta and England, 2006; Behrens and Bostock, 2023). Meanwhile, terrestrial conditions are also influenced by the strength and

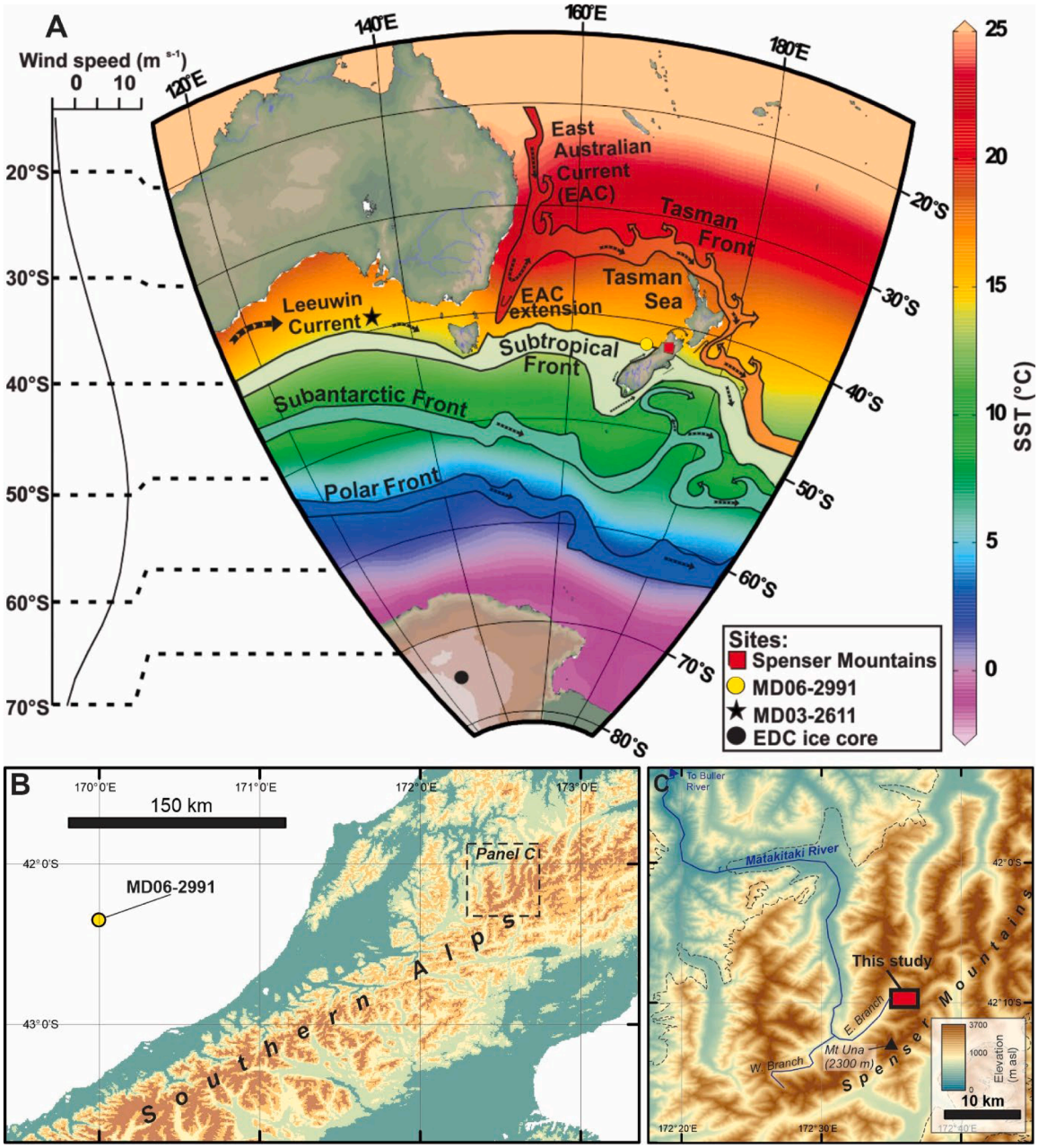

Fig. 1. (A) Location of our marine and terrestrial study sites within the context of regional oceanic and atmospheric circulation in the southwest Pacific and Southern Oceans; (B) relative positions of marine and terrestrial sites; (C) topographic situation of our terrestrial site in the Spenser Mountains.

position of the southern westerly winds via the position and intensity of the mid-latitude storm track (Gillett et al., 2006).

Our aim is to provide quantitative reconstructions of sea surface and air temperature change through the last glacial termination. We use assemblages of planktic foraminifera in marine sediment core MD06-2991, recovered from the eastern Tasman Sea, to quantify SST changes through the last glacial termination (Fig. 1). Onshore, and directly downwind of our marine sediment core site, we apply cosmogenic surface exposure dating and numerical glacier modelling to reconstruct the timing and climatic significance of glacier length changes in the Spenser Mountains of New Zealand's Southern Alps. Together, these closely-spaced marine and terrestrial palaeoclimate records provide complementary records of past change in the regional atmosphere-ocean system. The proxy responses are supported by global climate model simulations, which enables evaluation of the drivers and mechanisms of millennial-scale climate change in the southern hemisphere during the last glacial termination.

2. Methods

2.1. Climate reconstruction from glaciers

2.1.1. Study site

Our terrestrial study site is an unnamed, west-facing cirque basin situated on the main range of the Spenser Mountains located ~2km NNW of Mt Humboldt (2206 m asl). The Spenser Mountains are a NNE–SSW-trending range situated at the northern margin of the Southern Alps and comprise Triassic-age semischist, sandstones, and mudstones of the Rakaia Terrane (Rattenbury et al., 2006). The study cirque is a tributary of the Matakitaki River East Branch that feeds the Buller River, which drains westward to the Tasman Sea (Fig. 1).

Today the Spenser Mountains are largely unglacierised, except for small glacierets/niche glaciers which exist in topographic hollows or beneath high peaks (Baumann et al., 2021). End-of-summer snowline observations since the late 1970s report average summer equilibrium line altitudes that lie between 2000 and 2150 m asl (Chinn, 1995). This indicates that the local equilibrium line altitude is proximal to the highest summit elevations around the study catchment, which exceeds 2160 m asl. Our chosen site preserves a sequence of moraines that clearly delineate the margin of the former glacier during separate advance or stillstand events since the Last Glacial Maximum. Based on their relative morphostratigraphic relationships, we distinguish these moraine sets with letters A (oldest) through to E (youngest).

2.1.2. Cosmogenic ^{10}Be dating

We collected 23 samples of moraine boulders for cosmogenic ^{10}Be surface exposure dating (Figs. 2, 3 Table 1). All samples were extracted using a portable rock saw, hammer, and chisel. We measured topographic shielding using a compass and digital clinometer. We recorded sample locations using a Trimble GeoXH global positioning system, which were differentially corrected using the Land Information New Zealand PositioNZ Post Processing Service, with average precision of 0.7 m and 0.4 m in the vertical and horizontal, respectively.

All samples were processed in the Victoria University of Wellington Cosmogenic Laboratory. We separated quartz from bulk rock samples using standard mechanical, magnetic, and chemical protocols and inspected its purity by solution ICP-MS. We added 0.27–0.29 mg ^{9}Be (carrier = VUW-PK1) to each sample prior to dissolution in concentrated HF. Beryllium was isolated using ion-exchange chromatography and selectively precipitated as $Be(OH)_2$ at pH 9. Samples were then calcined over an open flame, mixed with Nb, and packed into cathodes for measurement by accelerator mass spectrometry. Samples were processed in three batches, each with a procedural blank (Table S1).

Beryllium isotopic ratios of all samples and blanks were measured using the 14UD accelerator mass spectrometer at Australian National University against the NIST SRM4325 standard (assumed $^{10/9}$Be ratio = 3.0×10^{-11}). Beryllium ratios of the procedural blanks were internally consistent (Table S1). We blank-corrected our sample ratios using the arithmetic mean and standard deviation of three process blanks ($1.55 \pm 0.60 \times 10^5$ ^{10}Be atoms).

Fig. 2. Example photos of moraine boulders sampled for ^{10}Be cosmogenic surface exposure dating in the Spenser Mountains with their individual exposure ages computed as described in the methods.

We calculate exposure ages using the online exposure age calculator formerly known as the CRONUS-Earth online exposure age calculator, version 3 (Balco et al., 2008; available: http://hess.ess.washington.edu/). We assume a uniform sample density of 2.65 g cm^{-3} – a standard value for crystalline rock. As we preferentially selected samples that displayed no obvious signs of surface erosion, results are presented that assume zero sample erosion since deposition by the former glacier. For reference, applying an erosion rate of 2 mm kyr^{-1} would increase our exposure ages by ~350 yr and would not alter our conclusions.

Our samples are situated in a narrow elevation band, 1600–1700 m above sea level (Table 1), which is above the elevation of the regional winter snowline. Continuous automated snowpack measurements at a site situated 15 km north of our study cirque (Mahanga Ews, 1995 m asl) for the past six years indicate a maximum winter snow depth of ~0.5–1 m at that location (C. Zammit, National Institute of Water and Atmospheric research (NIWA), pers. comm.). Burial by 1 m of typical density (ρ = 0.2 g cm^{-3}) snow for 6 months of the year would reduce local production rates (thus increasing our exposure ages) by ~5 % relative to

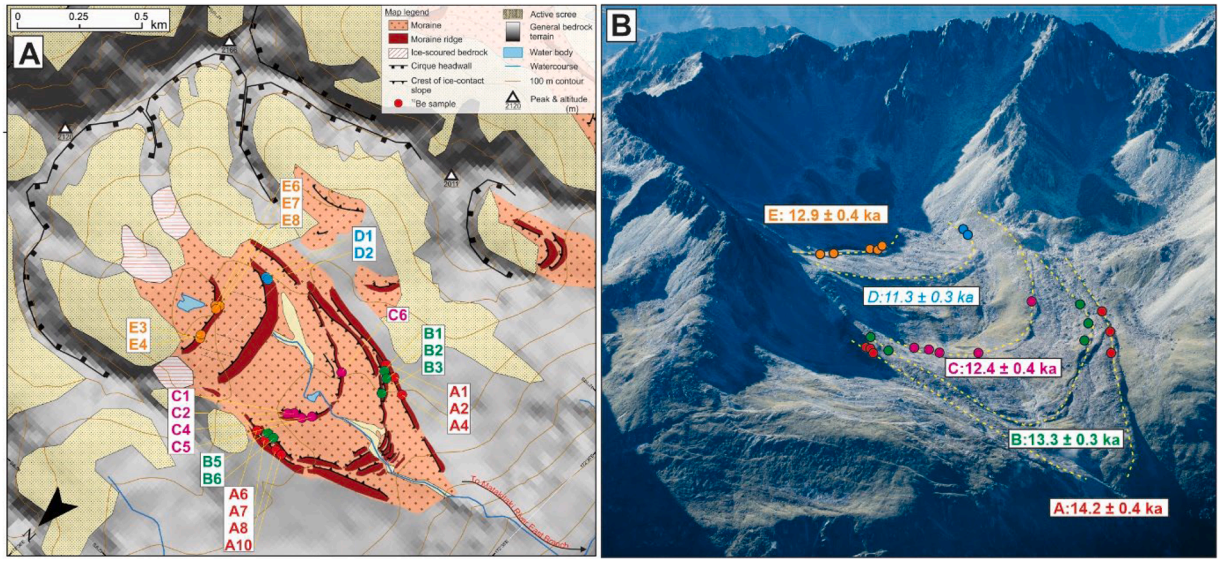

Fig. 3. (A) Geomorphic map depicting moraine distribution at the Spenser Mountains cirque site and individual sample locations across the 5 moraine belts (A–E); (B) An oblique aerial overlain by summary moraine ages (weighted mean (± 1 std. dev) exposure ages are given for each moraine set). Photo taken early autumn 2015, facing southeast (Source: Huw Horgan).

Table 1
Geographical and analytical data for the samples from the Spenser Mountains organised by moraine belt (A–E). ^{10}Be concentrations are reported relative to NIST SRM4235, with an assumed isotopic ratio of 3.00×10^{-11}. Exposure ages are calculated using the 'Macaulay' ^{10}Be calibration set (Putnam et al., 2010b) and the 'LSDn' scaling model (Lifton et al., 2014).

Batch #	ID	Lat (dd)	Lon (dd)	Elevation (m a.s.l)	Boulder dimensions (m) (m)			Quartz mass (g)	^{9}Be (mg)	Thickness (cm)	Shielding	^{10}Be ± 1s.d. (10^5 at^{-1} g)	Exposure age (ka)
					L	W	H						
1	A1	-42.162	172.594	1625.4	3.0	3.0	3.0	24.183	0.289	1.3	0.983	2.33±0.11	14.7 ± 0.7
1	A2	-42.162	172.593	1612.9	1.7	1.6	1.0	12.137	0.289	2.2	0.980	2.21±0.14	14.2 ± 0.8
1	A4	-42.162	172.592	1597.9	2.7	2.2	0.6	9.181	0.285	1.9	0.986	2.30±0.16	14.8 ± 1.0
1	A7	-42.157	172.595	1630.8	1.9	0.9	0.6	13.150	0.290	1.1	0.981	2.06±0.13	13.0 ± 0.8
1	A8	-42.157	172.594	1624.3	2.0	1.1	0.9	8.134	0.289	1.9	0.986	2.13±0.17	13.5 ± 1.1
1	A10	-42.157	172.594	1618.4	2.1	1.5	1.0	9.871	0.290	1.4	0.987	2.39±0.16	15.0 ± 1.0
1	B1	-42.162	172.593	1620.3	4.0	2.5	1.3	13.854	0.292	2.5	0.984	1.94±0.12	12.5 ± 0.8
1	B2	-42.162	172.593	1613.7	3.0	1.9	1.0	31.586	0.290	1.0	0.990	2.16±0.10	13.6 ± 0.6
1	B3	-42.161	172.593	1602.3	4.0	3.9	2.4	32.479	0.290	0.7	0.988	2.25±0.10	14.3 ± 0.6
2	B5	-42.157	172.595	1637.1	1.5	0.4	0.5	27.217	0.269	1.8	0.987	1.96±0.09	12.4 ± 0.6
2	B6	-42.157	172.595	1633.1	3.0	1.5	0.9	28.231	0.270	1.1	0.985	2.13±0.10	13.4 ± 0.7
2	C1	-42.158	172.595	1599.0	1.3	1.2	0.6	14.099	0.270	1.8	0.978	1.90±0.11	12.5 ± 0.8
2	C2	-42.158	172.595	1594.2	1.3	0.9	0.4	20.243	0.270	2.1	0.980	1.90±0.10	12.5 ± 0.7
2	C4	-42.159	172.595	1591.8	3.0	1.3	1.0	17.973	0.270	1.9	0.984	1.86±0.11	12.3 ± 0.7
3	C5	-42.159	172.594	1583.9	0.7	0.5	0.3	1.871	0.270	1.2	0.981	2.75±0.47	17.7 ± 3.0
3	C6	-42.161	172.595	1611.3	5.0	3.5	3.0	22.747	0.269	2.2	0.981	1.83±0.10	12.0 ± 0.7
3	D1	-42.161	172.601	1702.4	1.2	0.6	0.5	16.088	0.270	1.4	0.967	1.71±0.11	*10.8 ± 0.6*
3	D2	-42.161	172.600	1700.9	1.6	0.7	0.5	23.123	0.270	1.5	0.967	1.93±0.11	*12.0 ± 0.7*
3	E3	-42.158	172.601	1712.9	1.8	1.1	1.0	21.292	0.270	1.9	0.971	2.27±0.13	13.6 ± 0.8
3	E4	-42.158	172.601	1714.7	4.3	1.1	0.9	20.474	0.270	1.9	0.973	2.11±0.11	12.7 ± 0.7
3	E6	-42.159	172.601	1696.6	2.0	1.5	1.3	13.941	0.270	2.0	0.969	5.81±0.28	*34.2* ± 1.7
3	E7	-42.159	172.601	1700.3	2.4	1.3	1.3	20.454	0.270	1.1	0.969	2.19±0.12	13.2 ± 0.7
2	E8	-42.159	172.601	1701.1	4.0	2.3	1.6	19.836	0.270	1.7	0.969	2.02±0.11	12.4 ± 0.7

the no shielding case. Based on the topographic salience of our boulders we consider this scenario unlikely and suggest that the influence of snow shielding on our results is negligible (<2 %) relative to the analytical uncertainties. We therefore present our ages without any correction for snow cover.

We calculate exposure ages using the local 'Macaulay' (New Zealand) ^{10}Be production rate calibration dataset of Putnam et al. (2010b) and the Lifton et al. (2014); 'LSDn' scaling scheme. This production rate calibration is underpinned by robust independent radiocarbon constraints and internally consistent ^{10}Be measurements and was demonstrated to be accurate for regional applications over the last 18 ka (Putnam et al., 2010). Furthermore, the relatively close proximity of the calibration site to that of our study minimizes the impact of scaling-model uncertainties for our application. Application of the recent global calibration effort of Borchers et al. (2016) does not alter the mean moraine ages outside of the analytical uncertainty (Table S2). Thus, our conclusions are unaffected by our choice of production rate.

2.1.3. *Glacier modelling*

We conducted numerical glacier simulations using a coupled mass balance and ice-flow model (e.g. Doughty et al., 2013; Eaves et al., 2016, 2017, 2019; Muir et al., 2023). The mass balance model computes snow

accumulation using a simple temperature-threshold approach (snow--rain threshold set to 1 °C) and ablation is derived by solving the full energy balance equation using mean (AD 1981–2010) monthly climate observations (temperature, precipitation, incoming solar radiation, wind speed and relative humidity). As in our previous applications, the vertically-integrated ice-flow model uses the shallow ice approximation. We use this formulation for computational efficiency and acknowledge that the assumptions underpinning this approximation are less valid in mountainous domains. However, we note that comparisons between the shallow ice approximation and higher-order ice-flow formulations show little difference (Le Meur et al., 2004).

Our glacier-modelling experiments are designed to achieve two objectives: (1) to constrain the temperature anomaly, relative to present, under which the former ice geometries existed, as delineated by the dated moraines; and (2) to quantify the magnitude, if any, of temperature change required to explain retreat between moraine sets. To achieve these objectives, we conduct multiple 5000-yr simulations, each with a single temperature anomaly (relative to present), ΔT, which is applied uniformly across the year (e.g. no change in seasonality). ΔT for individual simulations are spaced at 0.1 °C intervals between -1.5 °C and -3.0 °C (inclusive). In each simulation, air temperature is varied interannually about the constant mean and we track glacier length changes that result from this climate noise.

To answer objectives 1 and 2, we analyse the resultant time series of annual glacier length and compare the outputs to the moraine positions. Moraine sets B–E include near-complete nested recessional moraines, which clearly indicate the former glacier terminus position. A terminal moraine is not preserved for moraine set A, therefore we infer glacier length using the model output from the 300-year equilibrium simulation (see above) that best fits the lateral moraine margins of moraine set A. Objective 1 is answered by identifying simulations where the observed moraine position falls within the range of the maximum and mean glacier length (Fig. 4), as this is the zone of highest moraine preservation potential in a noisy, constant climate. For objective 2, we examine the number of moraines encompassed by the maximum-mean range of glacier lengths. We focus on these times of greater-than-average terminus positions as we consider that moraines formed during any retreat periods, without a change in the mean climate, will eventually be destroyed as the glacier tends back towards its average length. If more than one moraine falls in the simulated mean-maximum range, then we consider that these moraines could have been formed due to glacier length changes produced by climatic noise alone (i.e. without a climatic change). In contrast, simulations that produce a glacier length range that intercepts only one moraine indicate that the mean climate changed to produce the glacier length changes preserved in the moraine record.

Each simulation is preceded by a 300-yr 'spin-up', where the glacier is evolved to its equilibrium geometry for the given temperature anomaly (ΔT), where ΔT is constant for every year of the simulation (i.e. no interannual noise is applied). During the next 5000 yr of each simulation, air temperature and the precipitation rate are varied interannually about constant means (equal to ΔT and ΔP). The amplitude of interannual variability in a 48-yr record of temperature and precipitation measurements are from a nearby weather station ('Lake Rotoiti 2'; -41.808, 172.842, 634 m asl, AD1958–2006; NIWA CliFlo Database, available: https://cliflo.niwa.co.nz/): $\sigma(T)$ = 0.45 °C and $\sigma(P)$ =14 % (both variables are 1 σ). We repeat these experiments with twice the variability of present day (i.e. $\sigma(T)$ = 0.9 °C and $\sigma(P)$ =28 %), in order to test the sensitivity of our results to this parameterisation. For direct comparability, each 5000-yr simulation forced with interannual variability uses the same time series of interannual perturbations, which have been randomly selected from a normal distribution. In all simulations mass balance and ice geometry are recalculated at the end of each model year.

2.2. Sea surface temperature reconstruction

We reconstruct sea surface conditions spanning the end of the Last Glacial Maximum and through the last glacial termination (22–10 ka) using planktic foraminiferal assemblages from the MD06-2991 giant piston core, extracted from the Challenger Plateau during the joint New

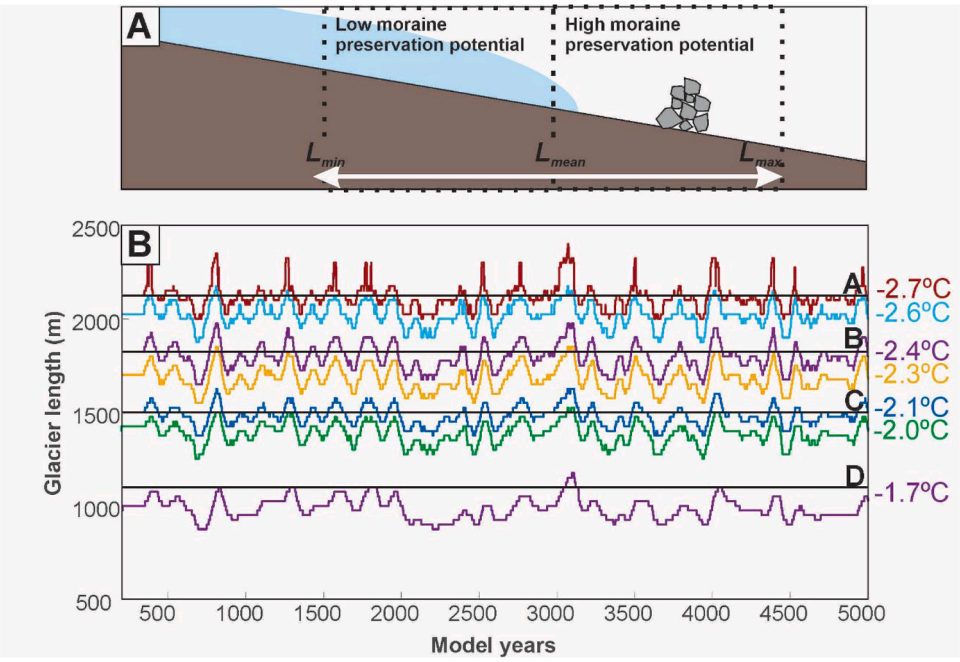

Fig. 4. Air temperature anomaly estimates derived from glacier modeling. (A) Schematic illustration of moraine preservation potential relative to glacier length (L); (B) Glacier lengths simulated for different temperature anomalies (ΔT) relative to present, when interannual air temperature ($\sigma(T)$ = 0.45 °C) and precipitation ($\sigma(P)$ = 14 %) variability are imposed. For clarity, experiments are only shown for cases where the average-maximum ($[L_{mean}\ L_{max}]$) range of simulated glacier length coincides with the position of dated moraines (shown as black horizontal lines). No simulations produced a 2D ice geometry that fit the planform geometry of the E moraine.

Zealand/French 2006 MATACORE voyage (Proust et al., 2008). The core site is situated in the eastern Tasman Sea, c. 100 km offshore the west coast of South Island New Zealand (Fig. 1). The core sits just north of the Subtropical Front today and is not influenced directly by the Southern Ocean and the Antarctic Circumpolar Current.

Planktic foraminiferal assemblages were counted from the >150 μm size fraction from 27 samples. Approximately 300 (range 206–377) whole or nearly whole planktic foraminiferal tests were identified and counted. Nineteen species of planktic foraminiferal taxa were discriminated and used in the reconstruction of mean annual SSTs. Following the methods of Hayward et al. (2012) and Cortese et al. (2013), we derive quantitative SST using both Modern Analog Technique (MAT) and random forest model transfer functions with reference to the 1223 Southern Hemisphere core top database (Cortese et al., 2013).

The age-depth model for the MD06-2991 core is constrained by 15 radiocarbon dates spanning 27–1 cal. ka BP (with 7 in the range 20–10 ka) on mixed planktic foraminifera (Fig. 5; Ryan et al., 2016), using the Marine20 calibration curve (Heaton et al., 2020). We sampled the core at variable resolution (every 1–10 cm), focussing the higher resolution sampling on the ACR interval where we achieve temporal resolution of 200–400 yr per sample.

3. Results

3.1. Glacier chronology

The A- and B-moraines represent the outermost moraines preserved in the cirque (Fig. 3). The A moraines comprise two prominent (~5 m high) continuous lateral moraine ridges. At their upstream end these moraines are oriented parallel to the B-moraines, with the latter situated immediately inboard. We distinguish between the A- and B-moraine sets by the fact that the A-moraines extend to 1450 m asl, whereas the B-moraines curve towards the valley floor, converging at ca. 1550 m asl, thus representing a smaller ice mass than delineated by the A moraines. The B moraines comprise multiple, nested moraines. Both A- and B-moraines display boulder ridge tops, with individual clasts set in a sand-silt matrix. Ice-proximal and ice-distal slopes of the moraines are partially vegetated by low alpine grasses. Six boulders sampled from the A-moraines return an error-weighted mean of 14.2 ± 0.4 ka ($n = 6$; no outliers). Meanwhile five boulders from the B-moraines yield an error-weighted mean age of 13.3 ± 0.3 ka (n = 5).

The C-moraines form a single, low (1–2 m high) broken moraine loop that encloses a small tarn (Fig. 3). Alpine grasses cover the left lateral component of this loop with few visible clasts, except for one large (~4 m high) boulder embedded in the crest (sample C6; Fig. 2). The former

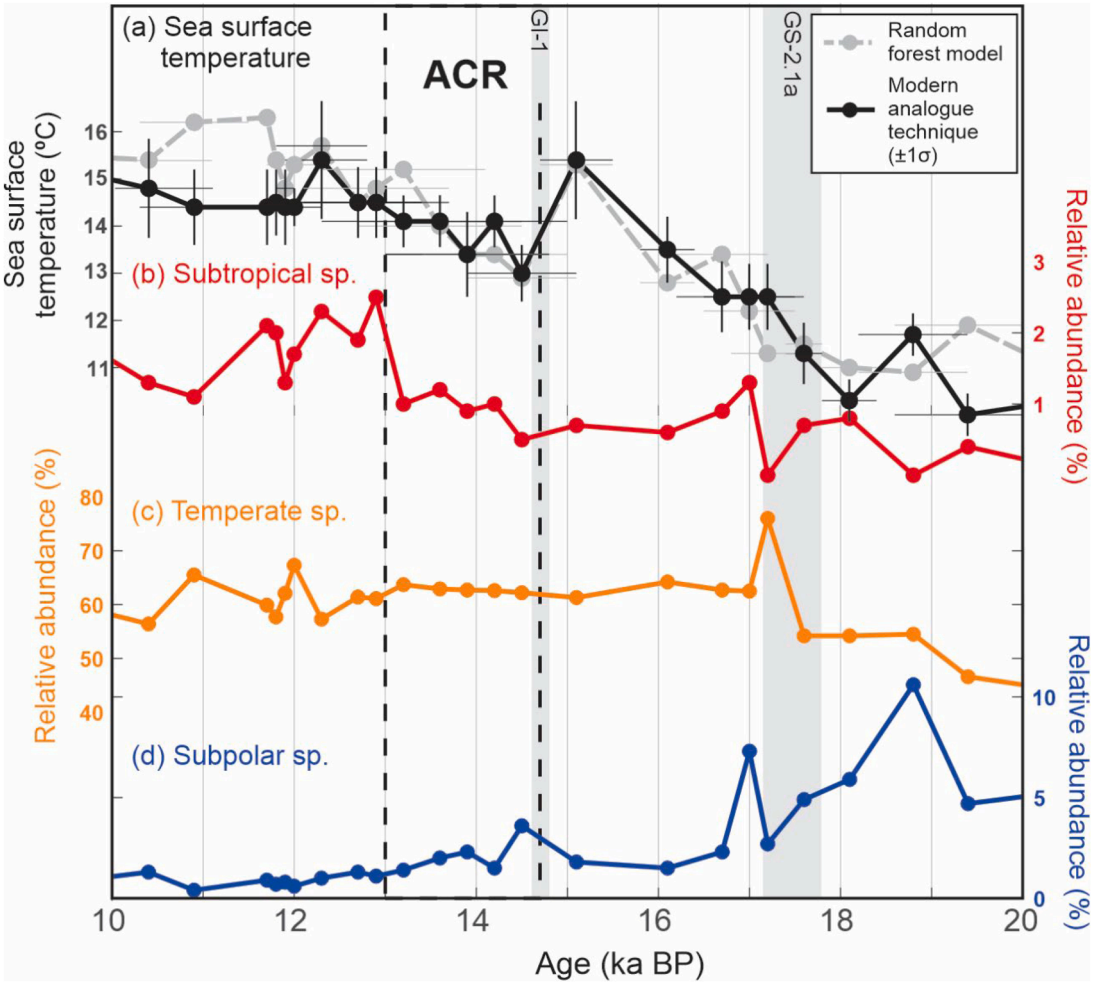

Fig. 5. Deglacial foraminifera assemblage and sea surface temperature (SST) reconstruction for MD06-2991. (a) SST derived from planktonic foraminifera using the modern analogue technique (MAT) and random forest (RF) model (Methods) with 1σ age model uncertainties. (b–d) Relative abundance of subtropical, temperate, and subpolar species (assemblages defined by Carter et al. (2008)). Black triangles denote radiocarbon ages used for age model construction of core MD06-2991 (Ryan et al., 2016). Vertical grey bars denote timing of major climate transitions in Greenland Ice Core Stratigraphy (Rasmussen et al., 2014), which are accompanied by intensity changes in the Atlantic Meridional Overturning Circulation (AMOC): Greenland Stadial 2.1a (GS-2.1a; 17.5 ± 0.3 ka) and Greenland Interstadial 1 (GI-1) transition (14.7 ± 0.2 ka).

glacier terminus is delineated at the valley centre (~1580 m asl) by a low (c. 1 m) boulder ridge with no discernible matrix. The right lateral component of the C-moraine loop is vegetated to a similar degree to the left side but punctuated more frequently at the surface by moraine boulders. Five samples from the C-moraine yield an error-weighted mean of 12.4 ± 0.4 ka (n = 5; no outliers).

The D-moraine is a continuous, relatively wide (10–20 m), bouldery, unvegetated terminal moraine that delineates a former ice mass that terminated at c. 1660 m asl (Fig. 3). We interpret the furrowed surface of much of the moraine, and lack of distinct ridge crest, to represent past mobility of the landform under periglacial conditions. At the true left end, the moraine is situated against the side wall of the valley and displays a more distinct ridge crest than in the valley centre. We collected samples from two boulders on the true-left portion of the moraine that returned an average age of 11.3 ± 0.3 ka ($n = 2$).

At the head of the cirque, the E-moraines form a continuous belt delineating a small ice mass that terminated at c. 1800 m asl (Fig. 3). The moraine set comprises a single continuous ridge, with smaller moraine ridges, of similar composition, nested within. There is no vegetation cover on this feature and the moraine comprises large (2–5 m long axis), interlocking boulders, with no observable matrix. The population of exposure ages from E-moraine are tightly clustered, with only 1 obvious outlier (E6; Table 1), which returned an age that was ~20 kyr greater than the population mean. Removal of this outlier yields an error-weighted mean of 12.9 ± 0.4 ($n = 4$; 1 outlier removed).

The ^{10}Be age of the D moraine is >2 σ younger than the E moraine, which violates relative ages of these landforms as indicated by their geomorphic relationship. The 'E' moraine returns an age that is indistinguishable from the C moraine at 1σ uncertainty. The D moraine age is based on only two ages from small boulders, which we consider may be erroneously young due to post-depositional disturbance (e.g. surface erosion, exhumation) or emplacement after moraine formation, such as by rockfall from the adjacent hillslope (Fig. 2). We thus interpret that moraines C, D, and E were deposited within centuries of one another at ~12.7 ± 0.6 ka (average of C and E moraines).

In summary, the ^{10}Be chronology from this site shows that the former cirque glacier at this site was most extensive at 14.2 ± 0.4 ka (Fig. 3). Subsequent retreat was punctuated by several re-advances/still-stands of the glacier terminus that deposited moraines B–E. The cirque deglaciated after 12.7 ± 0.6 ka and has since remained ice-free.

3.2. Glacier modelling

Our simulations show that the 'A' moraines (~14.2 ka) align with glacier margins in simulations where mean annual temperature is 2.6 to 2.7 °C lower than present (Fig. 4, Table 2). Meanwhile the simulated glacier reaches the 'B' moraines (~13.3 ka) when the mean air temperature anomaly is -2.3 to -2.4 °C and the 'C' moraines (~12.7 ka) temperature is -2.0 to -2.1 °C below present. The simulated glacier terminates over the 'D' and 'E' moraine sites in simulations when air temperature is set to 1.7 °C and 1.5 °C lower than present, respectively (Fig. 4).

Table 2
Summary ^{10}Be exposure ages and glacier-model derived palaeotemperature anomaly estimates for moraines A–E in the Spenser Mountains cirque. The range of temperature anomalies is derived from simulations where interannual temperature and precipitation anomalies are set to modern and 2x modern as defined by a nearby weather station.

Moraine set (relative age)	Age (ka)	Palaeotemperature anomaly (°C rel. to present)
A (oldest)	14.2 ± 0.4 (n = 6)	-2.5 to -2.7
B	13.3 ± 0.3 (n = 5)	-2.3 to -2.2
C	12.4 ± 0.4 (n = 5)	-2.1 to -1.9
D	*11.3 ± 0.3 (n = 2)**	-1.7
E (youngest)	12.9 ± 0.4 (n = 4)	warmer than -1.7

* Exposure age violates relative moraine age dictated by geomorphology and is interpreted to be anomalously young

Glacier simulations provided close fits to each moraine-defined outline except for the E moraine, which may represent the increased importance of local topoclimatic factors for maintaining this small former glacier. While our mass balance model accounts for topographic shading, other local processes such as redistribution of snow by wind and gravity, are not included. Such factors are increasingly important for defining mass balance distribution as glacier size decreases (Dadic et al., 2010). We interpret the good agreement between our simulations and other moraine defined limits (e.g. A–D) to represent dominance of larger-scale climate variables (e.g. temperature and precipitation), in determining mass changes over these larger ice geometries.

We find that glacier length (L) fluctuates by 50–100 m (1 σ) in response to interannual climate variability alone, when the amplitude of temperature and precipitation is prescribed similar to modern observations ($\sigma(T) = 0.45$ °C; $\sigma(P) = 14$ %), which represents 3–5 % of the average glacier length during the 5000-yr simulation. No simulation produced a mean-maximum range ($[L_{mean}\ L_{max}]$) of glacier length that encompassed more than one mapped moraine set. This result indicates that 0.5–0.7 °C warming is necessary to explain glacier retreat between the A–C moraines (Fig. 4). This result further suggests glacier retreat after deposition of the C-moraine, which occurred within dating uncertainties at ~12.7 ka, occurred in response to further warming of >0.3 °C.

Previous glacier modelling work has shown that the amplitude of interannual climate variability correlates with the amplitude of glacier length changes (Malone et al., 2019). Thus, if climate was more variable in the past, then glacier length changes due to interannual variability may have been larger, potentially encompassing more than one moraine set. Consistent with previous studies, we find that glacier variability is greater ($\sigma(L)$ = 120–160 m; 7–12 % of the mean) with higher amplitude climate variability. Again, no simulation produces a $[L_{mean}\ L_{max}]$ range of glacier lengths that encompasses more than one mapped moraine set, however several are short by just one grid cell (Fig. S1; Table S4), which suggests that perhaps pairs of adjacent moraines could have formed in a constant, but high-variability (twice present-day) climate. No one simulation produces a mean-max range of glacier length fluctuations that encompass more than two moraine sets. We thus conclude that change in the mean climate state is necessary to explain the net retreat of ice in the Spenser Mountains between 14.2 and 12.7 ka. The magnitude of warming across the last part of the termination indicated by this high-amplitude experiment is between 1.0 and 1.2 °C (Table 2).

3.3. Sea surface temperature reconstruction

Subpolar species (*Neogloboquadrina pachyderma; Turborotalita quinqueloba*) decline in abundance from 20 ka (Fig. 5; age-model and SST data provided in Table S3). This is followed by increases in temperate (*Globoconella inflata*) and subtropical species (*Globigerinoides ruber*) between 18.1 ka to 15.1 ka (Fig. 5). Both the MAT and random forest model SST estimates using the foraminiferal assemblages suggest a 5 °C rise over this interval, reaching close to the modern SST over the core site by 15.1 ± 0.4 cal. ka BP (Fig. 5). The deglacial warming trend is then reversed, with an increase in subpolar species abundance at the expense of subtropical species, representative of a ~2 °C reduction in SST (Fig. 5). The SST minimum during the temperature reversal occurs at 109.25 cm core depth, which is well constrained by a radiocarbon date at 110.25 cm (15.1 ± 0.2 cal. ka BP; 26) and has a modelled age of 14.5 ± 0.6 cal. ka BP (Fig. 5). Following this marked SST reduction, subtropical species gradually increase, before increasing sharply at ~13.2 ± 0.9 ka. These assemblage changes reflect a gradual recovery of SST

during and after the ice-core defined ACR time interval, with near-modern conditions regained by ~12.3 ± 0.5 ka.

4. Discussion

4.1. Deglacial climate proxy records in the southwest Pacific

Our new climate proxy data indicate close coupling of glacier length changes and SST in the New Zealand region throughout the last glacial termination. Two SST transfer functions applied to our planktonic foraminifera assemblages from MD06-2991 indicate net SST warming of 4–5 °C in the eastern Tasman Sea between 18 ka and 15 ka (Fig. 5). This warming likely represents the southward migration of the subtropical front over the core site (Bostock et al., 2015) and coincides with widespread deglaciation of the Southern Alps (Barrell et al., 2019). Previous glacier modelling studies indicate glacier retreat occurred in response to a corresponding air temperature increase of at least 4 °C between 18 and 15 ka (Putnam et al., 2013; Eaves et al., 2017; Fig. 6). The total magnitude of glacier retreat during this interval is difficult to constrain using geomorphic indicators. However, if air temperature in New Zealand tracked local SSTs closely throughout the last glacial termination, then glaciers in the Southern Alps may have retreated to near-pre-industrial extents by as early as ~15.5 ka.

A temperature reversal at our southwest Pacific core site occurs within the interval 15.1 ± 0.4 and 14.2 ± 0.8 ka BP. Formation of the outermost moraines in the Spenser Mountains cirque at ~14.2 ± 0.4 ka occurred synchronously, within dating uncertainties, with this SST minimum. Gradual warming then ensued, with a 1 °C SST increase recorded in MD06-2991 during the ACR.

On land, our glacial chronology indicates that the interval 14.2–13 ka was characterized by net glacier retreat (Fig. 4), consistent with warming of the adjacent ocean surface. The pattern of glacier change during the ACR found at the Spenser Mountains site mirrors that seen in other well-dated moraine records from the central Southern Alps where outer moraines first deposited c. 14–14.5 ka, followed by minor retreat and deposition of inner moraines at c. 13 ka (Putnam et al., 2010a; Tielidze et al., 2023).

Our numerical glacier modelling experiments suggest that an air temperature increase of at least 1 °C can explain the net retreat of the former cirque glacier in the Spenser Mountains during the ACR, which is consistent with snowline-based estimates from Tielidze et al. (2023). The reconstructed air temperature anomalies rely on the assumption that both seasonality and interannual variability of air temperature and precipitation at our study site was similar to that present during the ACR. Existing evidence from proxy and climate models indicate that any differences in seasonality during the ACR were modest in the New Zealand region (Vandergoes et al., 2008; Pedro et al., 2016), especially relative to millennial-scale events in the North Atlantic region (e.g. Denton et al., 2005; Schenk et al., 2018). Thus, it is unlikely that our assumption of seasonally uniform temperature change impacts our results. Furthermore, based on the close agreement of this air temperature rise with the independent SST data, and the high temperature-sensitivity of New Zealand glaciers (Mackintosh et al., 2017; Lorrey et al., 2022), we suggest that glacier retreat in New Zealand during the ACR was driven by a progressive and minor air temperature increase, rather than any significant precipitation change.

Continuous terrestrial climate proxy archives offer complementary insight to the structure of deglacial air temperature changes in this region. Pollen-based temperature reconstructions from the Southern Alps have suggested broad alignment with Antarctic temperature changes during the ACR (Newnham et al., 2012; Fig. 6). Furthermore, temperature reconstructions from chironomid assemblages in a high-altitude tarn in the central Southern Alps indicate high-amplitude (~3 °C) centennial-scale variability during the ACR (Vandergoes et al., 2008; Fig. 6). Initial cooling in the record occurs between 14.5–14.0 ka, with similar events centred on 13.6 ka and 13.4 ka (Fig. 6). The timing and amplitude of chironomid temperature changes, exhibit good agreement with the Southern Alps glacier record, indicating that regional air temperature declined within the first centuries of this millennial-scale cold interval.

4.2. Deglacial climate drivers in the southwest Pacific

A key question that arises from our new climate-proxy data concerns the cause of coupled air-sea cooling that occurred in the New Zealand region at ACR onset. The timing of this cooling event coincides with two globally-significant climate changes during the last glacial termination. First, Greenland ice cores record the abrupt onset of the Bølling-Allerød interstadial warming, which was followed approximately two centuries later by the onset of ACR cooling in Antarctica (Fig. 6; Jouzel et al., 2007; Rasmussen et al., 2014; WAIS Divide Project Members, 2015). Boreal warming at the Bølling-Allerød onset is widely considered to have been associated with intensification of AMOC (McManus et al., 2004), which increased the rate of northward, cross-equatorial heat flow in the Atlantic (Stocker and Johnsen, 2003; Pedro et al., 2016). Second, sea level markers record a phase of enhanced global mean sea level rise, known as Meltwater Pulse 1a (MWP1a; 14.5–14.0 ka; Lambeck et al., 2014) associated with melting continental ice sheets, which broadly coincided with the start of the Bølling-Allerød/ACR onset (Fig. 6).

Both abrupt AMOC recovery and an Antarctic contribution to MWP1a have been hypothesised as drivers of southern hemisphere cooling during the ACR (Weaver et al., 2003; Pedro et al., 2016). However, climate model simulations of large meltwater additions to the Southern Ocean from Antarctica tend to produce an abrupt, high-magnitude cooling over the ice sheet that is inconsistent with temperature proxy data from ice cores (Pedro et al. 2016). Temperature reconstructions from Antarctic ice cores typically indicate gradual, millennial-scale cooling during the ACR, rather than an abrupt temperature reversal (Fig. 6). These ice core data are reproduced in climate model simulations that do not prescribe Antarctic meltwater, but rather simulate the ACR as being driven solely by AMOC intensification (Pedro et al., 2016). Furthermore, the different structure of temperature response between Antarctica and our mid-latitude site makes it unlikely that early ACR cooling in New Zealand represents a response to enhanced meltwater from Antarctica.

Simulations of abrupt AMOC resumption conducted using Community Climate System Model version 3 (CCSM3; He, 2011) (in which AMOC resumption is triggered by cessation of freshwater flux into the North Atlantic with all other forcings held constant at 14.9 ka values—see Pedro et al. (2018) for more details), broadly reproduce the hemispheric-scale pattern and magnitude of ACR cooling associated with a large suite of field-based proxy data when integrated through to 13 ka (Pedro et al., 2016). Our regional temperature proxies from New Zealand indicate that any response of the climate system to AMOC changes during the ACR likely occurred within centuries of its intensification, rather than millennia. To test the physical plausibility of this rapid change inference, we analyse the transient response of our study region in climate model simulations (Fig. 7). We find that modelled SST in the Tasman Sea permanently departs the 1σ bounds of variability 50 yr after forced AMOC intensification, declining over the following 400 yr to a new equilibrium state with SSTs ~1.5 °C lower (Fig. 7a). We also observe that the spatial patterns of SST were heterogenous across southern mid- and high latitudes. Cooling is greatest along the northern margin of the Southern Ocean, particularly in the southern Indian Ocean and the Tasman Sea, and these regions also experience an enhanced tropical-mid latitude meridional thermal gradient (Fig. 7b).

Pedro et al. (2018) identified several mechanisms by which climate signals arising from AMOC intensification are propagated throughout the global climate system. First, there is an abrupt response of the atmosphere, which occurs within the first decades of AMOC recovery and is manifest in the southern hemisphere as an equatorward shift in the position of the mid-latitude westerlies (e.g. Pedro et al., 2016; Buizert

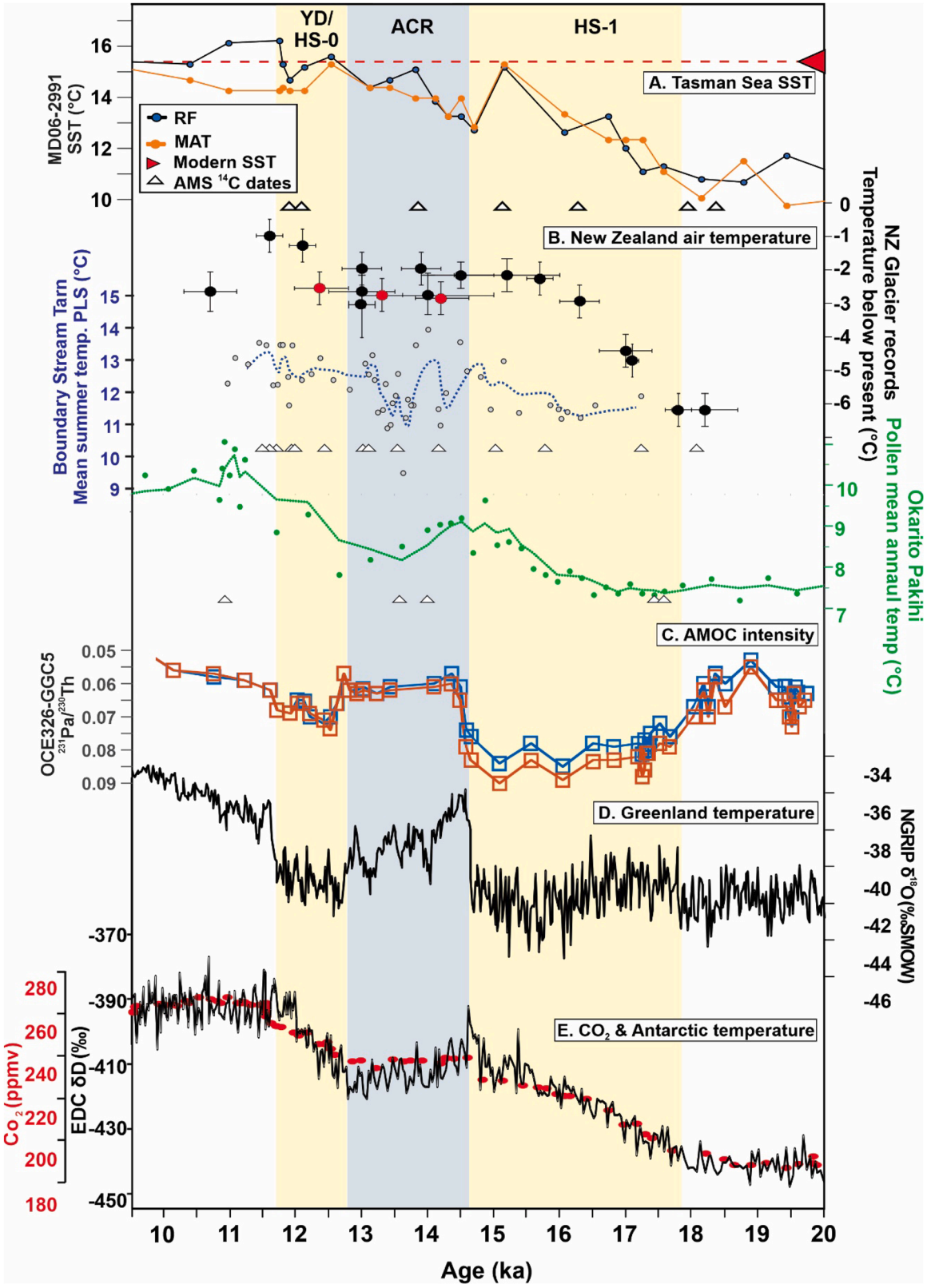

Fig. 6. (A) Regional SST reconstructions for the Tasman Sea (this study); (B) compiled air temperature reconstructions derived from numerical glacier modelling of moraine sequences in the Southern Alps (Doughty et al., 2013; Kaplan et al., 2013; Putnam et al., 2013; Eaves et al., 2017, with A, B, and C moraines from this study shown in red), the chironomid summer temperature record of Vandergoes et al. (2008) and the pollen-derived mean annual temperature reconstruction from Okarito Pakihi (Newnham et al., 2012); (C) Atlantic meridional overturning circulation intensity proxy of sedimentary $^{231}Pa/^{230}Th$ from deep western subtropical Atlantic (OCE326-GGC5; McManus et al., 2004); (D) EPICA Dome-C temperature (Jouzel et al., 2007) and CO_2 measurements (Lourantou et al., 2010) on the AICC2012 age model; and (E) Greenland temperature (Rasmussen et al., 2014). Vertical bar 14.6–12.8 ka indicates the Antarctic cold reversal.

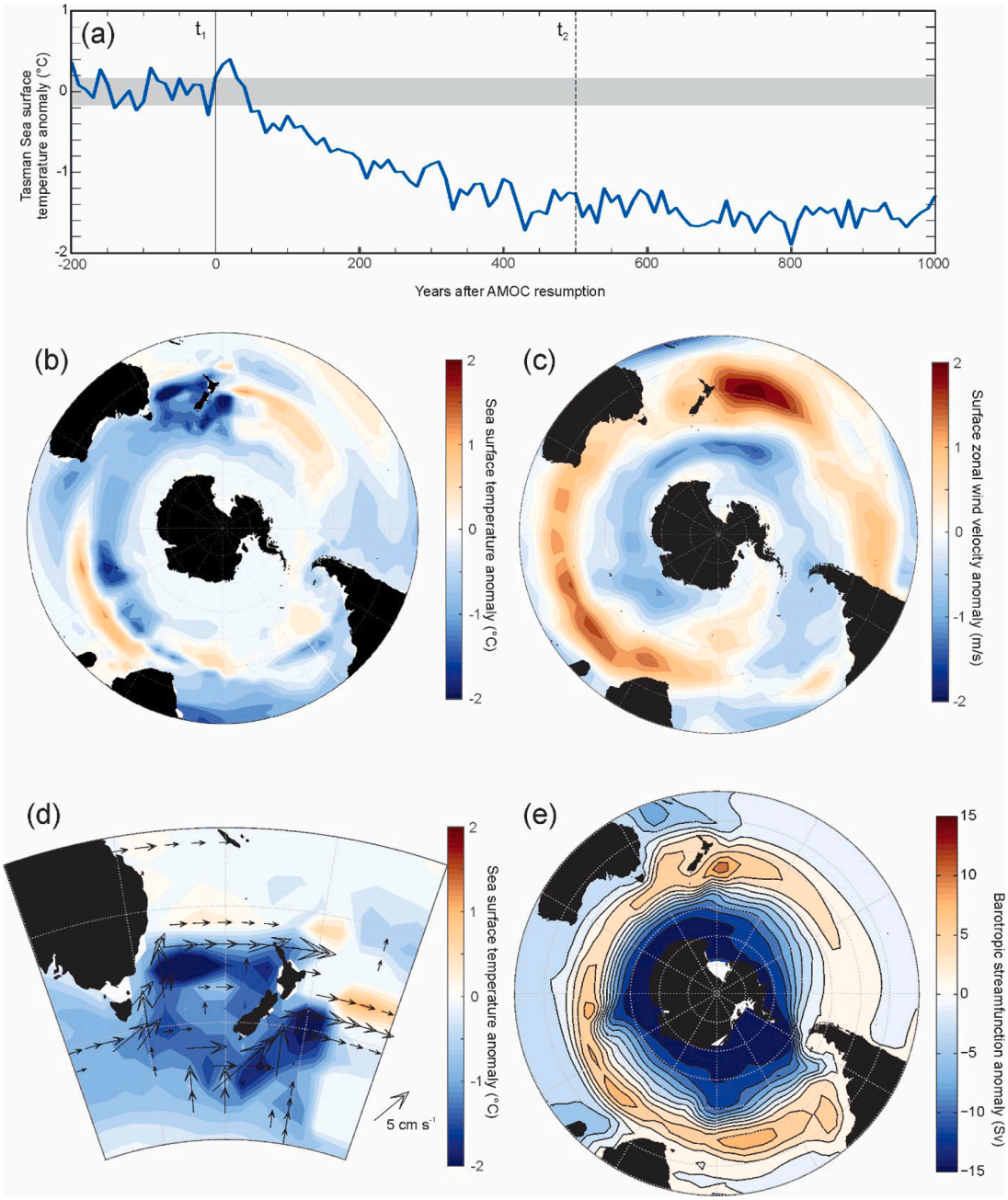

Fig. 7. Climate anomalies 500 yr after a forced intensification of Atlantic meridional overturning circulation (AMOC) using the Community Climate System Model version 3 (Pedro et al., 2018): (a) Tasman Sea surface temperature time series. Horizontal grey bar delineates the 1 s.d. SST variability range in the century prior to AMOC recovery. (b) sea surface temperature; (c) surface zonal wind speed; (d) sea surface velocity in the Tasman Sea region (only shown are anomalies >95 % significance, according to a student's T-Test) overlain on SST anomalies; (e) barotropic stream function.

et al., 2018). Second, onset of deep-water production in the North Atlantic causes a shoaling of the Atlantic thermocline. This thermocline adjustment is propagated within decades to the Pacific Ocean via Kelvin and Rossby waves (Huang et al., 2000; Pedro et al., 2018), where it contributes to surface cooling. Third, increased northward heat transport by the AMOC cools the South Atlantic over several centuries, which spreads eastwards by advection of cold surface water across southern mid-latitudes on the northern side of the ACC. The sign of temperature change in the New Zealand region, as indicated by our climate proxy data, is directly consistent with the last of these inferred atmosphere-ocean teleconnection impacts from changes in AMOC.

We note that the spatial pattern of SST change and surface ocean currents in the Tasman Sea region, as well as elsewhere at southern mid-latitudes (Fig. 7), closely resembles idealised model results of Denton et al. (2021) for the Zealandia Switch. In their study, Denton et al. (2021) examine the changes linked to meridional shifts of the southern westerly winds in isolation, which emphasised that altered wind stress over the South Pacific gyre modulates heat flux to the Tasman Sea. It is well documented that the CCSM3 simulations induce strengthening of the subtropical jet in response to AMOC intensification at the ACR onset (Pedro et al., 2016; Fig. 7c). The CCSM3 model results show alteration of wind stress impacts on southern hemisphere ocean circulation and heat distribution occurs in a manner consistent with the Zealandia Switch hypothesis. In both the Pacific and Indian oceans, the greatest SST changes coincide with the southern margin of the East Australian and Agulhas western boundary currents, respectively (Fig. 7b). These

poleward-flowing currents deliver warm, subtropical water to the southern mid-latitudes that replaces water advected eastwards by wind-driven subtropical gyres. An enhanced subtropical jet in response to AMOC intensification (Fig. 7; Pedro et al., 2016, 2018) increases the meridional wind stress curl gradient between 30 °S and 50 °S in the central Pacific and Indian oceans, which weakens and shifts the southern edge of subtropical gyres in both ocean basins (Fig. 7e), likely due to enhanced northward Ekman transport (e.g. Behrens and Bostock, 2023). In both the Tasman Sea and the southwest Indian Ocean, changes to both ocean gyres reduce southward extension and eastward retroflection of western boundary currents, which contributes to SST changes both north and south of the subtropical front (Fig. 6b). In the southwest Pacific, there is intensification of the Tasman Front at the expense of the East Australian Current extension (Fig. 7d), leading to simultaneous warming of the southern South Pacific gyre and Tasman Sea cooling, respectively (Fig. 7b). These patterns are consistent with the Zealandia Switch hypothesis, but occur within a global climate model experiment specifically designed to investigate AMOC change impacts consistent with the bipolar seesaw hypothesis.

The Zealandia Switch hypothesis was proposed to operate over orbital timescales to explain ice age terminations, with consideration that millennial change for glaciers and ice sheets might also accord with the same mechanism (Denton et al., 2021; Putnam et al., 2023). However, only an insolation-based driver was proposed, which leaves open the question of what may trigger the Zealandia Switch during abrupt millennial-scale climate events such as the ACR. Our observations suggest that the Zealandia Switch mechanisms outlined by Denton et al. (2021) may be an integrated component of the coupled atmosphere-ocean response that is connected to AMOC-induced climate changes at centennial-millennial timescales.

5. Conclusion

Glacier and marine evidence show close coupling between air and SSTs in the southwest Pacific during the last deglaciation. Both air and SST proxies from the Tasman Sea region record: (i) warming during Heinrich Stadial 1 (c. 18–15 ka), with SST reaching near modern values; (ii) air and SST minima are reached within centuries of the abrupt intensification of AMOC that coincides with the ACR/Bølling-Allerød onset, followed by (iii) gradual warming with near-modern ocean temperatures reached by ~12.7 ka. Analysing the transient response of the climate system to AMOC perturbations, we observe that the Tasman Sea responds sensitively over centennial-timescales, as illustrated by a strong temperature response relative to other locations in the southern mid-latitudes. The rate and spatial pattern of temperature change for the Tasman Sea region following AMOC intensification indicates an important role for both oceanic and atmospheric teleconnections of southern mid latitude climate. Our findings suggest that aspects of the proposed Zealandia Switch mechanism may be linked with dynamical elements of the AMOC-driven bipolar seesaw hypothesis, and the associated teleconnections arising from it, which may explain late-glacial millennial-scale climate change in the southern hemisphere.

CRediT authorship contribution statement

Shaun R. Eaves: Writing – review & editing, Writing – original draft, Visualization, Project administration, Methodology, Investigation, Funding acquisition, Formal analysis, Conceptualization. **Andrew N. Mackintosh:** Writing – review & editing, Supervision, Project administration, Investigation, Funding acquisition, Conceptualization. **Joel B. Pedro:** Writing – review & editing, Supervision, Investigation, Conceptualization. **Helen C. Bostock:** Writing – review & editing, Supervision, Investigation, Funding acquisition, Formal analysis, Conceptualization. **Matthew T. Ryan:** Writing – review & editing, Visualization, Investigation, Formal analysis. **Kevin P. Norton:** Writing – review & editing, Supervision, Investigation, Funding acquisition, Conceptualization. **Bruce W. Hayward:** Investigation, Formal analysis. **Brian M. Anderson:** Writing – review & editing, Software, Funding acquisition, Conceptualization. **Feng He:** Writing – review & editing, Resources, Investigation, Funding acquisition, Conceptualization. **Richard S. Jones:** Writing – review & editing, Investigation. **Andrew M. Lorrey:** Writing – review & editing, Resources. **Rewi M. Newnham:** Writing – review & editing, Supervision. **Stephen G. Tims:** Writing – review & editing, Formal analysis. **Marcus J. Vandergoes:** Supervision, Resources.

Declaration of competing interest

The authors declare that they have no known competing financial interests or personal relationships that could have appeared to influence the work reported in this paper.

Data availability

Data will be made available on request.

Acknowledgements

This work was funded by a New Zealand Antarctic Research Institute (NZARI), Royal Society of New Zealand Marsden Fund (contract VUW1701), Australian Institute of Nuclear Science and Engineering (AINSE) Award No. ALNGRA1116, and a Leverhulme Study Abroad Studentship. JBP received funding from the Carlsberg Chrono-Climate project and from the Australian Government. ANM and RSJ were partly supported by Australian Research Council (ARC) SRIEAS grant SR200100005, Securing Antarctica's Environmental Future. F.H. was supported by the US NSF (OPP-1834667) and the Climate, People, and the Environment Program. Support for this research was also provided by the University of Wisconsin-Madison Office of the Vice Chancellor for Research and Graduate Education with funding from the Wisconsin Alumni Research Foundation. We would like to acknowledge high-performance computing support from Yellowstone (ark:/85065/d7wd3xhc) and Cheyenne (doi:10.5065/D6RX99HX) provided by NCAR's Computational and Information Systems Laboratory, sponsored by the National Science Foundation. This research used resources of the Oak Ridge Leadership Computing Facility at the Oak Ridge National Laboratory, which is supported by the Office of Science of the U.S. Department of Energy under Contract No. DE-AC05-00OR22725. We would like to acknowledge Dr Helen Neil at NIWA for access to the MD06-2991 core, which was funded by a joint New Zealand/French collaboration on the RV Marion Dufresne (MATACORE).

Supplementary materials

Supplementary material associated with this article can be found, in the online version, at doi:10.1016/j.epsl.2024.118802.

References

Balco, G., Stone, J.O., Lifton, N.A., Dunai, T.J., 2008. A complete and easily accessible means of calculating surface exposure ages or erosion rates from 10Be and 26Al measurements. Quat. Geochronol. 3 (3), 174–195.

Barrell, D.J., Putnam, A.E., Denton, G.H., 2019. Reconciling the onset of deglaciation in the upper Rangitata valley, southern alps, New Zealand. Quat. Sci. Rev. 203, 141–150.

Baumann, S., Anderson, B., Chinn, T., Mackintosh, A., Collier, C., Lorrey, A.M., Rack, W., Purdie, H., Eaves, S., 2021. Updated inventory of glacier ice in New Zealand based on 2016 satellite imagery. J. Glaciol. 67 (261), 13–26.

Behrens, E., Bostock, H., 2023. The response of the subtropical front to changes in the southern hemisphere westerly winds—evidence from models and observations. J. Geophys. Res.: Oceans 128 (2), e2022JC019139.

Borchers, B., Marrero, S., Balco, G., Caffee, M., Goehring, B., Lifton, N., Nishiizumi, K., Phillips, F., Schaefer, J., Stone, J., 2016. Geological calibration of spallation production rates in the CRONUS-Earth project. Quat. Geochronol. 31, 188–198.

Bostock, H.C., Hayward, B.W., Neil, H.L., Sabaa, A.T., Scott, G.H., 2015. Changes in the position of the subtropical front south of New Zealand since the last glacial period. Paleoceanography 30 (7), 824–844.
Buizert, C., Sigl, M., Severi, M., Markle, B.R., Wettstein, J.J., McConnell, J.R., Pedro, J.B., Sodemann, H., Goto-Azuma, K., Kawamura, K., Fujita, S., 2018. Abrupt ice-age shifts in southern westerly winds and Antarctic climate forced from the north. Nature 563 (7733), 681–685.
Caesar, L., McCarthy, G.D., Thornalley, D.J.R., Cahill, N., Rahmstorf, S., 2021. Current atlantic meridional overturning circulation weakest in last millennium. Nat. Geosci. 14 (3), 118–120.
Carter, L., Manighetti, B., Ganssen, G., Northcote, L., 2008. Southwest pacific modulation of abrupt climate change during the antarctic cold reversal–younger dryas. Palaeogeogr. Palaeoclimatol. Palaeoecol. 260 (1-2), 284–298.
Chinn, T.J.H., 1995. Glacier fluctuations in the Southern Alps of New Zealand determined from snowline elevations. Arc. Alp. Res. 27 (2), 187–198.
Cortese, G., Dunbar, G.B., Carter, L., Scott, G., Bostock, H., Bowen, M., Crundwell, M., Hayward, B.W., Howard, W., Martínez, J.I., Moy, A., 2013. Southwest Pacific Ocean response to a warmer world: insights from Marine Isotope Stage 5e. Paleoceanography 28 (3), 585–598.
Dadic, R., Mott, R., Lehning, M., Burlando, P., 2010. Wind influence on snow depth distribution and accumulation over glaciers. J. Geophys. Res.: Earth Surface 115.
Denton, G.H., Alley, R.B., Comer, G.C., Broecker, W.S., 2005. The role of seasonality in abrupt climate change. Quat. Sci. Rev. 24 (10-11), 1159–1182.
Denton, G.H., Anderson, R.F., Toggweiler, J.R., Edwards, R.L., Schaefer, J.M., Putnam, A. E., 2010. The last glacial termination. Science (1979) 328 (5986), 1652–1656.
Denton, G.H., Putnam, A.E., Russell, J.L., Barrell, D.J., Schaefer, J.M., Kaplan, M.R., Strand, P.D., 2021. The Zealandia switch: ice age climate shifts viewed from southern hemisphere moraines. Quat. Sci. Rev. 257, 106771.
Denton, G.H., Toucanne, S., Putnam, A.E., Barrell, D.J., Russell, J.L., 2022. Heinrich summers. Quat. Sci. Rev. 295, 107750.
Ditlevsen, P., Ditlevsen, S., 2023. Warning of a forthcoming collapse of the Atlantic meridional overturning circulation. Nat. Commun. 14 (1), 1–12.
Doughty, A.M., Anderson, B.M., Mackintosh, A.N., Kaplan, M.R., Vandergoes, M.J., Barrell, D.J., Denton, G.H., Schaefer, J.M., Chinn, T.J., Putnam, A.E., 2013. Evaluation of lateglacial temperatures in the Southern Alps of New Zealand based on glacier modelling at Irishman Stream, Ben Ohau Range. Quat. Sci. Rev. 74, 160–169.
Eaves, S.R., Mackintosh, A.N., Anderson, B.M., 2019. Climate amelioration during the Last Glacial Maximum recorded by a sensitive mountain glacier in New Zealand. Geology 47 (4), 299–302.
Eaves, S.R., Mackintosh, A.N., Anderson, B.M., Doughty, A.M., Townsend, D.B., Conway, C.E., Winckler, G., Schaefer, J.M., Leonard, G.S., Calvert, A.T., 2016. The last glacial maximum in the central North Island, New Zealand: palaeoclimate inferences from glacier modelling. Clim. Past 12 (4), 943–960.
Eaves, S.R., Anderson, B.M., Mackintosh, A.N., 2017. Glacier-based climate reconstructions for the last glacial–interglacial transition: Arthur's Pass, New Zealand (43° S). J. Quat. Sci. 32 (6), 877–887.
Gillett, N.P., Kell, T.D., Jones, P.D., 2006. Regional climate impacts of the Southern Annular mode. Geophys. Res. Lett. 33 (23) https://doi.org/10.1029/2006GL027721.
Gupta, A.S., England, M.H., 2006. Coupled ocean–atmosphere–ice response to variations in the southern annular mode. J. Clim. 19 (18), 4457–4486.
Hall, A., Visbeck, M., 2002. Synchronous variability in the southern hemisphere atmosphere, sea ice, and ocean resulting from the annular mode. J. Clim. 15 (21), 3043–3057.
Hayward, B.W., Sabaa, A.T., Kolodziej, A., Crundwell, M.P., Steph, S., Scott, G.H., Neil, H.L., Bostock, H.C., Carter, L., Grenfell, H.R., 2012. Planktic foraminifera-based sea-surface temperature record in the Tasman Sea and history of the Subtropical Front around New Zealand, over the last one million years. Mar. Micropaleontol. 82, 13–27.
He, F., 2011. Ph.D thesis. Department of Atmospheric and Oceanic Sciences, University of Wisconsin-Madison, p. 161.
Heaton, T.J., Köhler, P., Butzin, M., Bard, E., Reimer, R.W., Austin, W.E., Ramsey, C.B., Grootes, P.M., Hughen, K.A., Kromer, B., Reimer, P.J., 2020. Marine20—the marine radiocarbon age calibration curve (0–55,000 cal BP). Radiocarbon 62 (4), 779–820.
Huang, R.X., Cane, M.A., Naik, N., Goodman, P., 2000. Global adjustment of the thermocline in response to deep water formation. Geophys. Res. Lett. 27 (6), 759–762.
Jouzel, J., Masson-Delmotte, V., Cattani, O., Dreyfus, G., Falourd, S., Hoffmann, G., Minster, B., Nouet, J., Barnola, J.M., Chappellaz, J., Fischer, H., 2007. Orbital and millennial Antarctic climate variability over the past 800,000 years. Science (1979) 317 (5839), 793–796.
Kaplan, M.R., Schaefer, J.M., Denton, G.H., Doughty, A.M., Barrell, D.J., Chinn, T.J., Putnam, A.E., Andersen, B.G., Mackintosh, A., Finkel, R.C., Schwartz, R., 2013. The anatomy of long-term warming since 15 ka in New Zealand based on net glacier snowline rise. Geology 41 (8), 887–890.
Lambeck, K., Rouby, H., Purcell, A., Sun, Y., Sambridge, M., 2014. Sea level and global ice volumes from the last glacial maximum to the holocene. Proc. Natl. Acad. Sci. 111 (43), 15296–15303.
Le Meur, E., Gagliardini, O., Zwinger, T., Ruokolainen, J., 2004. Glacier flow modelling: a comparison of the shallow ice approximation and the full-stokes solution. Comptes Rendus Phys. 5 (7), 709–722.
Lifton, N., Sato, T., Dunai, T.J., 2014. Scaling in situ cosmogenic nuclide production rates using analytical approximations to atmospheric cosmic-ray fluxes. Earth Planet. Sci. Lett. 386, 149–160.
Lorrey, A.M., Vargo, L., Purdie, H., Anderson, B., Cullen, N.J., Sirguey, P., Mackintosh, A., Willsman, A., Macara, G., Chinn, W., 2022. Southern Alps equilibrium line altitudes: four decades of observations show coherent glacier–climate responses and a rising snowline trend. J. Glaciol. 68 (272), 1127–1140.
Lourantou, A., Lavrič, J.V., Köhler, P., Barnola, J.M., Paillard, D., Michel, E., Raynaud, D., Chappellaz, J., 2010. Constraint of the CO2 rise by new atmospheric carbon isotopic measurements during the last deglaciation. Global Biogeochem. Cycles 24 (2).
Mackintosh, A.N., Anderson, B.M., Lorrey, A.M., Renwick, J.A., Frei, P., Dean, S.M., 2017. Regional cooling caused recent New Zealand glacier advances in a period of global warming. Nat. Commun. 8 (1), 1–13.
Malone, A.G., Doughty, A.M., Macayeal, D.R., 2019. Interannual climate variability helps define the mean state of glaciers. J. Glaciol. 65 (251), 508–517.
McManus, J.F., Francois, R., Gherardi, J.M., Keigwin, L.D., Brown-Leger, S., 2004. Collapse and rapid resumption of Atlantic meridional circulation linked to deglacial climate changes. Nature 428 (6985), 834–837.
Muir, R., Eaves, S., Vargo, L., Anderson, B., Mackintosh, A., Sagredo, E., Soteres, R., 2023. Late glacial climate evolution in the Patagonian Andes (44–47° S) from alpine glacier modelling. Quat. Sci. Rev. 305, 108035.
Newnham, R.M., Vandergoes, M.J., Sikes, E., Carter, L., Wilmshurst, J.M., Lowe, D.J., McGlone, M.S., Sandiford, A., 2012. Does the bipolar seesaw extend to the terrestrial southern mid-latitudes? Quat. Sci. Rev. 36, 214–222.
Pedro, J.B., Bostock, H.C., Bitz, C.M., He, F., Vandergoes, M.J., Steig, E.J., Chase, B.M., Krause, C.E., Rasmussen, S.O., Markle, B.R., Cortese, G., 2016. The spatial extent and dynamics of the Antarctic cold reversal. Nat. Geosci. 9 (1), 51–55.
Pedro, J.B., Jochum, M., Buizert, C., He, F., Barker, S., Rasmussen, S.O., 2018. Beyond the bipolar seesaw: toward a process understanding of interhemispheric coupling. Quat. Sci. Rev. 192, 27–46.
Putnam, A.E., Denton, G.H., Schaefer, J.M., Barrell, D.J., Andersen, B.G., Finkel, R.C., Schwartz, R., Doughty, A.M., Kaplan, M.R., Schlüchter, C., 2010a. Glacier advance in southern middle-latitudes during the Antarctic cold reversal. Nat. Geosci. 3 (10), 700–704.
Putnam, A.E., Schaefer, J.M., Barrell, D.J.A., Vandergoes, M., Denton, G.H., Kaplan, M. R., Finkel, R.C., Schwartz, R., Goehring, B.M., Kelley, S.E., 2010b. In situ cosmogenic 10Be production-rate calibration from the Southern Alps, New Zealand. Quat. Geochronol. 5 (4), 392–409.
Putnam, A.E., Schaefer, J.M., Denton, G.H., Barrell, D.J., Andersen, B.G., Koffman, T.N., Rowan, A.V., Finkel, R.C., Rood, D.H., Schwartz, R., Vandergoes, M.J., 2013. Warming and glacier recession in the Rakaia valley, Southern Alps of New Zealand, during Heinrich Stadial 1. Earth Planet. Sci. Lett. 382, 98–110.
Proust, J.N., Lamarche, G., Migeon, S., Neil, H., 2008. Climate and tectonic changes in the ocean around New Zealand. Eos. Trans. Am. Geophys. Union. 89 (31), 277–278.
Putnam, A.E., Denton, G.H., Schaefer, J.M., 2023. A 10Be chronology of the Esmark Moraine and Lysefjorden region, southwestern Norway: evidence for coeval glacier resurgence in both polar hemispheres during the Antarctic cold reversal. Quat. Sci. Rev. 316, 108259.
Rasmussen, S.O., Bigler, M., Blockley, S.P., Blunier, T., Buchardt, S.L., Clausen, H.B., Cvijanovic, I., Dahl-Jensen, D., Johnsen, S.J., Fischer, H., Gkinis, V., 2014. A stratigraphic framework for abrupt climatic changes during the Last Glacial period based on three synchronized Greenland ice-core records: refining and extending the INTIMATE event stratigraphy. Quat. Sci. Rev. 106, 14–28.
Rattenbury, M.S., Townsend, D.B., Johnston, M.R., (compilers), 2006. Geology of the Kaikoura area: scale 1:250,000 geological map. Lower Hutt: GNS Science. Institute of Geological & Nuclear Sciences, 1:250,000 geological map 13. 70 p + 1 folded map.
Ryan, M.T., Newnham, R.M., Dunbar, G.B., Vandergoes, M.J., Rees, A.B., Neil, H., Callard, S.L., Alloway, B.V., Bostock, H., Hua, Q., Anderson, B.M., 2016. Exploring the source-to-sink residence time of terrestrial pollen deposited offshore Westland, New Zealand. Rev. Palaeobot. Palynol. 230, 37–46.
Schenk, F., Väliranta, M., Muschitiello, F., Tarasov, L., Heikkilä, M., Björck, S., Brandefelt, J., Johansson, A.V., Näslund, J.O., Wohlfarth, B., 2018. Warm summers during the Younger Dryas cold reversal. Nat. Commun. 9 (1), 1634.
Stocker, T.F., Johnsen, S.J., 2003. A minimum thermodynamic model for the bipolar seesaw. Paleoceanography 18 (4).
Tielidze, L.G., Eaves, S.R., Norton, K.P., Mackintosh, A.N., Pedro, J.B., Hidy, A.J., 2023. Early glacier advance in New Zealand during the Antarctic cold reversal. J. Quat. Sci. 38 (4), 544–562.
Vandergoes, M.J., Dieffenbacher-Krall, A.C., Newnham, R.M., Denton, G.H., Blaauw, M., 2008. Cooling and changing seasonality in the Southern Alps, New Zealand during the Antarctic cold reversal. Quat. Sci. Rev. 27 (5-6), 589–601.
WAIS Divide Project Members, 2015. Precise interpolar phasing of abrupt climate change during the last ice age. Nature 520 (7549), 661–665.
Weaver, A.J., Saenko, O.A., Clark, P.U., Mitrovica, J.X., 2003. Meltwater pulse 1A from Antarctica as a trigger of the Bølling-Allerød warm interval. Science (1979) 299 (5613), 1709–1713.